


Please cite the Published Version

De Chowdhury, Swapnadip, Zhou, Jian G, Khait, Anatoliy, Causon, Derek, Qian, Ling , Mingham, Clive and Pullen, Tim (2023) Local overshoot and wind effects on wave overtopping at vertical coastal structures. Proceedings of the Institution of Civil Engineers: Maritime Engineering, 176 (1). pp. 3-13. ISSN 1741-7597

DOI: <https://doi.org/10.1680/jmaen.2020.33>

Publisher: ICE Publishing

Version: Accepted Version

Downloaded from: <https://e-space.mmu.ac.uk/627469/>

Usage rights:  In Copyright

Additional Information: Copyright © ICE Publishing 2021

Enquiries:

If you have questions about this document, contact openresearch@mmu.ac.uk. Please include the URL of the record in e-space. If you believe that your, or a third party's rights have been compromised through this document please see our Take Down policy (available from <https://www.mmu.ac.uk/library/using-the-library/policies-and-guidelines>)

Local overshoot and wind effects on wave overtopping at vertical coastal structures

S. De. Chowdhury, J. G. Zhou, A. Khait, D. Causon,
L. Qian, C. Mingham

Centre for Mathematical Modelling and Flow Analysis, Department
of Computing & Mathematics, Manchester Metropolitan University,
Manchester, M1 5GD, UK

T. Pullen

HR Wallingford, Wallingford OX10 8BA, UK

Wind effects on wave overtopping over a fully impermeable vertical sea wall are studied numerically using the open source CFD library OpenFOAM®. A pressure gradient correction term is incorporated in the momentum equations. In the range of wave conditions of the present studies, it is found that in the absence of wind, the increase of the wave steepness results in reduction of the wave overtopping. This is related to the instability of the standing wave formed at the front of a vertical structure. Such instability was noticed in the range of steepness between 0.285 and 0.443 from the previous physical experiments for a regular wave interacting with a vertical structure. In our numerical studies we confirm the existence of this regime. Our studies further show that the stability of the standing wave determines the shape and volume of the overshooting jet, which has a close effect on wave overtopping. When a wind is relatively weak, e.g. wind speed of 10m/s, it is unable to alter the shape and volume of the overshooting jet much, meaning a weak wind effect on wave overtopping. When a wind is strong, e.g. speed of 30m/s, it completely deforms the overshooting jet and volume, resulting in overtopping discharge almost 3 times of that without a wind.

1. Introduction

Many coasts are vulnerable to wind effects at moderate to high wind speeds during normal weather as well as a storm surge. Coastal defences are standard choices to protect the coasts against flooding from wave overtopping and yet still it is not usual to design them based on studies specifically focused on an understanding of wind effects. The primary reason is that the incorporation of a wind generation facility into an existing physical flume is not straightforward. De Waal *et al.* (1996) and Wolters and van Gent (2007) used paddle wheels rotated at a given speed to transport water spray generated due to the wave impact on the vertical structure. The wheel speed was calibrated to have enough time for the impinging water on the structure to rise up and then stick to the wheel blade. Under the assumption that all of the spray that is generated due to wave impact is blown onshore by the wind, these tests aimed to account for the wind effects on overtopping

in physical model tests. The tests suggested a high increase in overtopping rates by wind compared to no wind conditions in some specific types of wave impacts, although results could not be quantified fully due to the lack of proper scaling laws. González-Escrivá *et al.* (2004) reproduced a real storm surge event in a laboratory and reported a significant increase in overtopping rates due to wind especially on small overtopping rates. One can predict wind effects on overtopping (De Rouck *et al.* (2005)) using estimates from neural network models (van Gent *et al.* (2007)) based on a large database created from numerous physical model tests. This can give certain factors to scale the overtopping rates without wind to account for wind effects. However, sometimes it is hard to find a physical explanation behind this scaling. As there is no reliable empirical relations for accessing wind effects on wave overtopping, coastal engineers are left with prescribing a wide margin in the design of a coastal defence-height. This appears



Figure 1. Coastal defence failure due to one event at Torbay, UK. Courtesy: D. Stewart and M. Wood, Torbay council.

to be a normal choice for places with high onshore wind speeds in particular, but clearly less economical in practice. Relevant CFD simulations of wind induced wave overtopping might be useful for planning and designing coastal defences in areas prone to high wind speed in particular. For example, failure of coastal defence in one event at Torbay, UK is evidenced in Figure 1, where the road between Torquay and Paignton had to be closed due to extreme overtopping hazard followed by high onshore wind speed.

The topic of wind wave interactions is relatively well studied, see for example Miles (1957), Kharif *et al.* (2008), Chalikov (1978), Yan and Ma (2010), Xie (2014), Hasan *et al.* (2018), etc. A two-phase model is also developed by Hieu *et al.* (2014) and Li and He (2011) to study wind-wave interaction at the sea wall in two dimension under relatively small wind speeds. The problem of wind effects on wave overtopping can be thought of, in a sense, as a special class of the wind wave interaction problem. There are several mechanisms through which wind contributes to overtopping: (1) wind energy transfer to the waves in between successive run-ups; (2) curvature of the overshooting water due to the strong shear force from the wind after a strong wave impact and (3) wind driven surface currents in shallow waters. Mechanism (1) is mostly found in the case of a mildly sloped or curved structure, whereas, for a vertical seawall causing strong reflection of the incident waves, mechanism (2) is dominant. There are few studies (for example see Ward *et al.* (1996, 1998)) focused on (1) where in some cases wind effects on run up and overtopping on slopes are clearly visible, especially at high wind speeds. Mechanism (2) by its nature leads to more violent wave structure interactions

than the others and was considered by De Waal *et al.* (1996) and Wolters and van Gent (2007). During an extreme storm surge event mechanism (2) is seldom encountered. Moreover, it is relatively easier to understand the dynamics of wave impact which leads to overshoot in a normal windless condition, owing to significant progress in recent times in computational hydrodynamic modelling of violent wave structure interactions. The overshoot is the key source to enhance overtopping under wind effects and that is where we put the focus in this paper.

In the paper we describe the numerical model and discuss the methodologies adopted to introduce the desired wind speed into the computational model. Then we discuss the basis for choosing the parameters for the incident wave conditions. The numerical calculations performed with an aim to investigate the wind effects on wave overtopping are validated using the past experimental study of Kharif *et al.* (2008). Adjacent to the structure, we put specific focus on understanding the wave condition which leads to the high overshoot and how this overtopping jet is affected by wind speeds. Unless otherwise stated, the length and time scales are normalized by the offshore water depth d and $\sqrt{d/g}$, respectively, i.e. $\hat{x} = x/d$ and $\hat{t} = t/\sqrt{d/g}$ (in other words, a variable with hat denotes nondimensionalization by these rules), where $g = 9.81\text{m/s}^2$ is the only non zero vertical component of the vector \mathbf{g} representing the acceleration due to gravity. The wind velocity is retained in dimension since it can not be Froude scaled.

2. Statement of the problem

In this section we describe the details of the set up we use for our computational investigation followed by a discussion of how we introduce the wind effect in the model.

2.1. The numerical model

We use the open source CFD library OpenFOAM[®] in order to simulate wind effects on the wave overtopping. OpenFOAM solves Reynolds-Averaged Navier-Stokes (RANS) equations, which in vector form read:

$$(1) \quad \nabla \cdot \mathbf{u} = 0,$$

$$(2) \quad \frac{\partial \rho \mathbf{u}}{\partial t} + \nabla \cdot (\rho \mathbf{u} \mathbf{u}) - \nabla \cdot \boldsymbol{\tau} = -\mathbf{g} \cdot \mathbf{x} \nabla \rho - \nabla p_d,$$

where \mathbf{u} is the velocity vector having three components, \mathbf{x} is the radius vector in a Cartesian coordinate system, ρ is the density of the air and water mixture. The pseudo-dynamic pressure $p_d = p - \rho \mathbf{g} \cdot \mathbf{x}$ is the static pressure minus the hydrostatic component. The stress tensor is

$$(3) \quad \tau = (\mu + \mu_t) [\nabla \mathbf{u} + (\nabla \mathbf{u})^T],$$

where μ is the dynamic viscosity and μ_t is the turbulent viscosity to be determined from the appropriate semi-empirical turbulence model. It is important to note that the turbulence model is applied in cases when the air or water flows are strongly turbulent in the entire computational domain. In our case, the effects of turbulence are significant only in the small region where the wind flow is induced numerically (see below). In other regions of the domain, the turbulence is weak and cannot be accounted for using semi-empirical turbulence models, thus we select $\mu_t = 0$.

The motion of the two-phase mixture of water and air with the sharp interface between the phases is taken into account using the Volume of Fluid (VOF) technique by solving the phase fraction equation:

$$(4) \quad \frac{\partial \alpha}{\partial t} + \nabla \cdot \mathbf{u} \alpha + \nabla \cdot (\mathbf{u}_r \alpha (1 - \alpha)) = 0.$$

Here the volume fraction α is bounded within $[0, 1]$ with value 0 referring to a dry cell and 1 to a wet cell. Any value within the range refers to a cell at the air-water interface. The third term in (4) introduces an artificial compression that helps to maintain the air-water interface sharp by selecting $|\mathbf{u}_r| = \min [c_\alpha |\mathbf{u}|, \max (|\mathbf{u}|)]$ with the appropriate compression factor c_α . The density of mixture in (1) - (2) is $\rho = \alpha \rho_w + (1 - \alpha) \rho_a$, where ρ_w and ρ_a are densities of water and air respectively. The Finite Volume Method (FVM) was used to solve the equations (1) - (4).

Within the conventional approach, the wind above the water waves is introduced by selection of appropriate boundary conditions that lead to the air flow across the entire computational domain. This approach is computationally inefficient when wind impact is important only within a certain area of the domain. Consequently, we induce the motion of the air with the velocity vector \mathbf{u}_{wind} by using an additional pressure gradient correction over the prescribed cell zone. This correction is applied only to a few selected cells in the computational domain, where the wind effect is found to be dominant (e.g., close to the coastal defence). The approach

helps to avoid very small time steps assuring the computation stability at Courant number $O(0.5)$. To explain the details of the pressure gradient correction method, we first consider the numerical procedures involved in the solution of the equations (1) - (3).

The peculiarity of the system (1) - (3) is the inability of its explicit solution with respect to pressure p_d , while conserving the mass according to (1). To overcome this problem, the so-called PISO algorithm is implemented in the OpenFOAM framework Issa (1985); Oliveira and Issa (2001). This algorithm consists of prediction and correction parts. Within the prediction step, vector equation (2) is presented in the matrix form:

$$(5) \quad \mathbf{A} \mathbf{u}^* - \mathbf{H} \mathbf{u}^* = -\mathbf{g} \cdot \mathbf{x} \nabla \rho - \nabla p_d,$$

where \mathbf{A} and \mathbf{H} are diagonal and off-diagonal matrices of coefficients that are obtained during the Finite Volume discretization of the model. This equation is solved to find the predicted velocity field \mathbf{u}^* determined by the “frozen” pressure field.

The second PISO step is introduced to correct both pressure and velocity fields in order to satisfy the mass and momentum conservation. At this step the equation (5) is presented in the form:

$$(6) \quad \mathbf{A} \mathbf{u}^{**} = \mathbf{H} \mathbf{u}^* - \mathbf{g} \cdot \mathbf{x} \nabla \rho - \nabla p_d^{**},$$

where \mathbf{u}^{**} and p_d^{**} are corrected values of the velocity and the pressure. To have the mass conservation it is required $\nabla \cdot \mathbf{u}^{**} = 0$ according to (1). Taking divergence of (6), the Poisson equation for the corrected pressure can be written:

$$(7) \quad \nabla \cdot (\mathbf{A}^{-1} \nabla p_d^{**}) = \nabla \cdot (\mathbf{A}^{-1} \mathbf{H} \mathbf{u}^* - \mathbf{A}^{-1} \mathbf{g} \cdot \mathbf{x} \nabla \rho).$$

Numerical solution of the Poisson equation (7) allows obtaining the corrected pressure p_d^{**} and the corrected velocity:

$$(8) \quad \mathbf{u}^{**} = \mathbf{A}^{-1} \mathbf{H} \mathbf{u}^* - \mathbf{A}^{-1} \mathbf{g} \cdot \mathbf{x} \nabla \rho - \mathbf{A}^{-1} \nabla p_d^{**}.$$

The solution of the equations (7) and (8) is enclosed into the loop; three iterations are usually enough to obtain the mass and momentum conservation at each time step.

As aforementioned, the method of pressure gradient correction was used to induce the wind in the area of the domain designated by Ω in Figure 2. Since the variables \mathbf{u}^{**} and p_d^{**} are coupled in the

PISO method by simultaneous solution of (7) and (8), any artificial change in one field leads to automatic update in another satisfying the conservation of mass and momentum. Therefore, it is required to modify only one of these two variables. In view of computational stability, the wind correction is introduced to the the velocity field \mathbf{u}^{**} after each PISO iteration to compute \mathbf{u}^{***} :

$$(9) \quad \mathbf{u}^{***} = \mathbf{u}^{**} + \chi \mathbf{s} [|\mathbf{u}_{\text{wind}}| - |\langle \mathbf{u}_{\text{s}}^{**} \rangle_{\Omega}|].$$

Here the difference in the absolute values of the velocities is taken along the wind direction defined by the unit vector $\mathbf{s} = \mathbf{u}_{\text{wind}}/|\mathbf{u}_{\text{wind}}|$. This allowed correction of the velocity field \mathbf{u}^{**} only in the wind direction \mathbf{s} , while remaining it unchanged in the perpendicular directions. The value of the velocity \mathbf{u}^{**} calculated in the PISO loop is first projected onto the wind direction, $\mathbf{u}_{\text{s}}^{**} = \mathbf{s} \cdot \mathbf{u}^{**}$, and then averaged over the region Ω :

$$(10) \quad \langle \mathbf{u}_{\text{s}}^{**} \rangle_{\Omega} = \frac{\sum_{\Omega} \mathbf{s} \cdot \mathbf{u}^{**} W}{\sum_{\Omega} W},$$

where W is the volume of each computational cell within the region Ω , while $\sum_{\Omega} W$ is the total volume of all cells in Ω . Since velocity correction given by (9) is executed at each PISO iteration, the relaxation factor χ was introduced to maintain the computation stability.

The velocity correction in the PISO loop is introduced by the corresponding pressure gradient in the following form: $\mathbf{u}^{**} \sim \mathbf{A}^{-1} \nabla p_d^{**}$, see (8). To be consistent with the PISO method, the equation (9) is rewritten in the following form:

$$(11) \quad \begin{aligned} \mathbf{u}^{***} &= \mathbf{u}^{**} + \mathbf{A}^{-1} \underbrace{\chi \mathbf{s} \langle \mathbf{A}^{-1} \rangle_{\Omega}^{-1} [|\mathbf{u}_{\text{wind}}| - |\langle \mathbf{u}_{\text{s}}^{**} \rangle_{\Omega}|]}_{\langle \nabla p_{\text{wind}} \rangle_{\Omega}} \\ &= \mathbf{u}^{**} + \mathbf{A}^{-1} \langle \nabla p_{\text{wind}} \rangle_{\Omega}, \end{aligned}$$

where $\langle \nabla p_{\text{wind}} \rangle_{\Omega}$ is the pressure gradient averaged over the region Ω and needed to maintain the required wind speed \mathbf{u}_{wind} . The values of the coefficients in the matrix \mathbf{A}^{-1} are averaged over the region Ω in the way similar to (10):

$$(12) \quad \langle \mathbf{A}^{-1} \rangle_{\Omega} = \frac{\sum_{\Omega} \mathbf{A}^{-1} W}{\sum_{\Omega} W},$$

As seen, in this method a single value of the pressure gradient $\langle \nabla p_{\text{wind}} \rangle_{\Omega}$ is introduced for the entire region Ω . In contrast to a cell-specific correction of the velocity, the introduced averaging technique avoids cell-to-cell fluctuations of the pressures and the

velocities due to the numerical instabilities possibly introduced by the explicit artificial modifications to the fields.

The main advantage of this approach is that the local wind speed in the air phase at the coastal structure is strictly prescribed to the value given as desired input wind speed. Thus, the need of accurate and demanding simulation of atmosphere boundary layer is circumvented leading to less computational effort. Outside the wind region, the flow is governed by the conditions imparted inside the wind region. For example, for the case of investigating wind effects on rogue waves (as considered in Appendix A to validate this approach), the flow beneath the wind region conforms to a physical sheltering effect (Figure 10). Sensitivity in the time history of overtopping rates recorded at the coastal structure with respect to the chosen length of the wind region Ω is reported in Appendix B.

The second-order schemes were used in FVM to discretize the spatial terms of the equations, while the time marching was done using the standard first-order Eulerian scheme. Within the structure of OpenFOAM, the framework named 'fvOptions' allows defining an external force to be imposed on the main solver, i.e. equations (1) - (4), without modifying the in-built PISO implementations. The desired region Ω can be defined as a `cellZone` and referred among other details like \mathbf{u}_{wind} , duration of the wind activity, the relaxation factor χ , etc. For a water wave simulation one key issue is wave generation at the inlet and its absorption at the outlet for carrying out simulations for a sufficiently long time. For that purpose in the present study, we use the set of libraries named waves2Foam (Jacobsen *et al.* (2012)). All the simulations are performed using the OpenFOAM ESI version 1706.

2.2. The computational domain

There are not many benchmark studies to verify a numerical model capable of dealing with wind effects on wave overtopping. A preliminary validation of the adopted numerical model is presented in De Chowdhury *et al.* (2019) using the experimental data from Ward *et al.* (1996). Another validation case could be based on the study of wind effects on the evolution of rogue waves, see for instance Yan and Ma (2010). Although this is not the precise topic we want to pursue in detail here, we have applied the above numerical model to this problem in Appendix A with the aim to validate our approach in simulation of the wind effects.

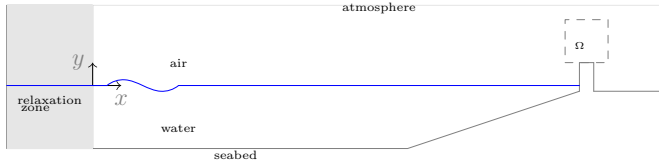


Figure 2. Schematic numerical wave tank used in the study

The Numerical Wave Tank (NWT) adopted for investigating overtopping under various conditions and wind effects is shown in Figure 2. We use regular monochromatic waves for all our cases with overtopping. The input wave with desired height H_o and length λ_o (the subscript 'o' stands for the offshore region) is prescribed at the inlet following the relaxation zone which houses both the wave generation and the absorption. The length of relaxation zone (i.e., spread along the x axis) is set as two times the maximum wave length we consider in our simulations. No slip boundary condition is used at the seabed and at the coastal defence, whereas, atmospheric boundary condition is used at the top of the domain with a constant pressure p . The wind zone Ω is upto the top of the domain starting just above the defence and covers its length; roughly extending upto five times the thickness of the overtopping jet at the coastal structure. The thickness of this jet is measured under similar input wave conditions but with no wind speed. Moreover, the geometry of the wind region is closely linked to the geometry of the coastal structure, see Figure 12 in Appendix B. The mesh structure in the neighbourhood of the coastal defence is rectangular since this structure is vertical with flat top in our case.

3. Standing wave stability

Traditionally the impulse parameter is used as a key to identify waves leading to impulse type interactions with overshoot at the vertical sea defence, see Bruce *et al.* (2018). The impulse parameter is given as

$$(13) \quad \mathcal{I} = \frac{h^2}{H\lambda},$$

where, h is the initial water depth at the seawall; H and λ are the wave height and length at the coastal defence, respectively. A generic definition for irregular waves is used in EurOtop manual, Van der Meer *et al.* (2018). We have conducted simulations to investigate wind effects on wave overtopping for a large number of test cases based on the incident wave condition. Details of

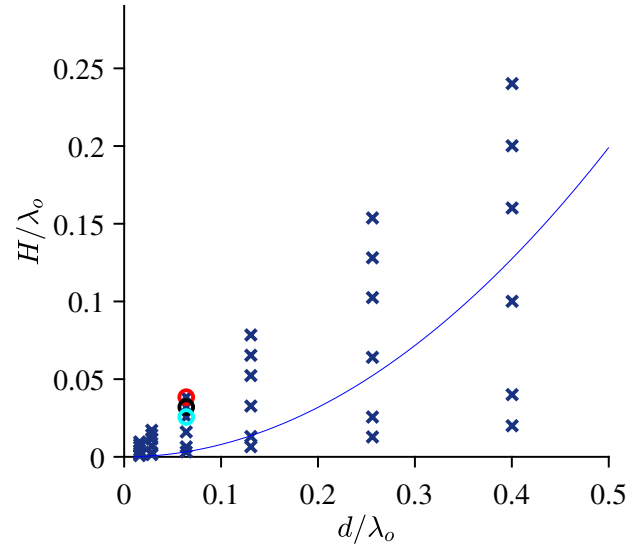


Figure 3. Summary of the test cases to investigate wind effects on wave overtopping. Individual cases are marked with \times .

the set-up and adopted mesh structure based on convergence are provided in Appendix B. A summary of these cases is presented in Figure 3. It is important to note here that the input parameter space in Figure 3 is defined using offshore wave parameters. Whereas, the impulse parameter is defined using parameters at the defence. Thus we use suitable transformations based on the wave elevation time history measured at the defence to incorporate the impulse parameter $\mathcal{I} = 0.23$ for $h/d \approx 0.7$ and $\hat{T} = 7$ in Figure 3 as a continuous curve. For $\mathcal{I} \leq 0.23$ the interaction of the incident wave with the sea defence is found to be impulse type in general. Cases for which the impulse parameter is higher than 0.23 (i.e., on the convex side of the curve in Figure 3) have very mild green water type overtopping, and wind effects do not appear to be dominant. For the points on the concave side of the curve, the overtopping is accompanied by a strong overshoot in the form of a vertical jet of water and wind effects are significant. Hence, we choose three cases of H/d being 0.3, 0.25 and 0.2 as shown in the figure using three circles of colours red, black and cyan, respectively. In these cases the non-dimensional period is $\hat{T} = 7$, i.e., consistent with the impulse curve. The other details of the three cases are summarized in Table 1, where the thickness Δ_{jet} of the overshooting jet is measured at the top (which is flat in our cases) of the sea defence at the time of overtopping. The wave steepness of the incident plus reflected wave system for all these three cases is different, meaning

H/d	Δ_{jet}/d	\mathcal{I}
0.3	0.1161	0.0529
0.25	0.1398	0.0636
0.2	0.1396	0.0794

Table 1. Details of the three impulse overshoot of incident waves with different wave heights.

we expect to observe different type standing waves at the time of overtopping. The shape of the overshooting jet depends on the underlying standing wave field and thus it is of some interest to investigate it in detail.

We can examine the stability of the standing wave formed due to a wave incident on a vertical sea wall by plotting the variation of the energy density of the standing wave over the wave steepness (i.e. ka , where k is the wave number and a is the wave amplitude), see Figure 4. The linear theory suggests that the wave energy $E = \rho g H^2/8$ grows quadratically without any specific upper bounds. However, with increasing wave steepness the waves tend to follow nonlinear behaviour and the linear assumptions become invalid. This is reflected up to certain extent in Figure 4 while using second-order standing wave theory which we adopt from [Chen et al. \(1988\)](#). While experimenting with standing waves on a vertical wall, [Longuet-Higgins and Drazin \(2002\)](#) have observed that in case of $ka < 0.285$ the waves are subcritical with the possibility of achieving a perfect steady state in overtopping cycles. Whereas, in the range $0.285 < ka < 0.443$, the incident plus reflected system becomes somewhat chaotic, which was referred as critical regime.

3.1. Wave interactions in the critical wave steepness regime

For our cases as listed in Table 1, only the case for which $H/d = 0.3$, i.e. $ka = 0.3063$, lays inside the critical regime reported by [Longuet-Higgins and Drazin \(2002\)](#). This is further supported by the predicted standing wave energy from our numerical simulation while compared to estimates by linear and second order wave theories as provided in Table 2. This shows that the energy in numerical simulation is nonlinear for the wave height considered and thus prone to instability owing to the wave steepness appearing inside the critical regime. Whereas, for other two cases where $H/d = 0.25$ and 0.2 , the steepness values $ka = 0.2565$ and 0.2060 lay inside the stability region. That means even though

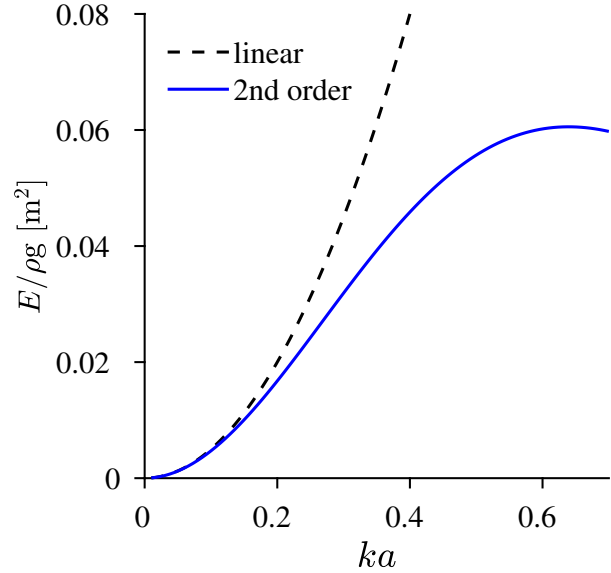


Figure 4. Variation of the standing wave energy over wave steepness.

	linear	second order	numerical
$E/\rho g \text{ [m}^2\text{]}$	9	8.137	7.8958

Table 2. Wave energy estimates by the present numerical simulations, linear and second-order theories for $H/d = 0.3$.

we expect to observe an overshoot for all these cases based on the impulse parameter, the shape of the jet may vary since the standing waves are in different stability regimes in terms of the wave steepness. This is shown in Figure 5 where we examine the time history of the wave elevation (i.e., η) measured at the vertical coastal structure. For the case of $H/d = 0.3$, we can clearly detect the characteristic triplet formation after initial cycles. We group these triplets as ψ_{ij} where index i is used to denote a specific triplet and index j is used to denote the wave inside this triplet. According to [Longuet-Higgins and Drazin \(2002\)](#), a major consequence of the standing waves in critical regime is that each third wave ($\psi_{13}, \psi_{23}, \dots$) of a triplet has the highest elevation compared to its neighbouring waves (i.e., the first waves $\psi_{11}, \psi_{21}, \dots$). For other cases (i.e., $H/d = 0.25$ and $H/d = 0.2$) where the standing wave is inside subcritical regime, this triplet does not form and overtopping takes place almost at steady rates in consecutive cycles.

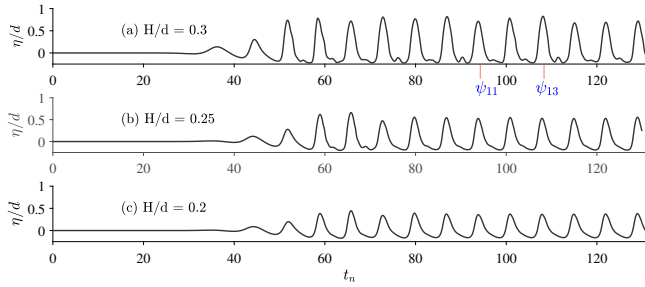


Figure 5. Time histories of the wave elevation measured at the vertical coastal structure.

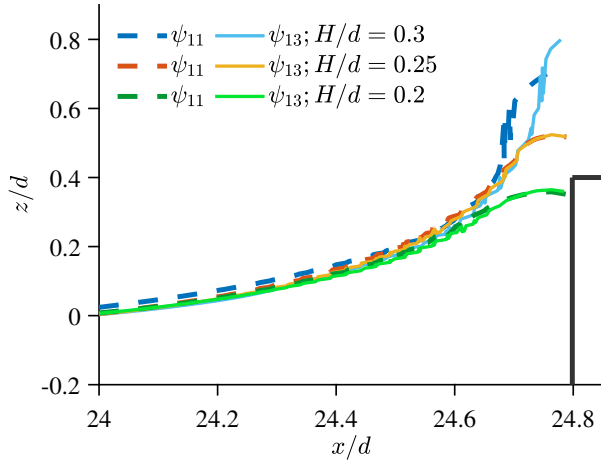


Figure 6. Form of the overtopping jets under critical and sub-critical wave steepness regimes. The vertical coastal structure (coloured in black) is located in right.

We can gain more insight into this phenomenon by studying the wave interactions in the same wave cycles, from which the results are depicted in Figure 6 demonstrating different degrees of overshooting jets. Unlike the other two cases in Figures 5 and 6, each third wave in the triplet for the case of $H/d = 0.3$ is characterized by the strongest overshoot followed by formation of cusps (with rounded top) with overturning in the preceding wave cycles.

3.2. Wind effects

The discussions above provide a base for interpretation of the increase in overtopping rates under different wind speeds in these cases. In order to help analysing results in the following section, we

introduce the Reynolds number as:

$$(14) \quad \text{Re}(u_{\text{wind}}) = \frac{\rho_a u_{\text{wind}} \Delta_{\text{jet}}}{\mu_a},$$

where u_{wind} is the only non-zero component of the prescribed horizontal wind velocity field inside the wind zone Ω , i.e. $\mathbf{u}_{\text{wind}} = \{u_{\text{wind}}, 0, 0\}$ and μ_a is the dynamic viscosity of air. The variation of overtopping rates over wave steepness is shown in Figure 7. Here, we nondimensionalize the overtopping rates q_{wind} and q_0 , i.e. overtopping rates with and without wind speed, respectively, with respect to the standing wave energy flux (i.e. $\mathcal{E}C$ where $\mathcal{E} = E/\rho g$ and C is the shallow water wave celerity). The overtopping rates are calculated based on time history of overtopping discharges $q(t)$ per unit crest width, i.e.,

$$(15) \quad q_{\text{wind},0} = \frac{1}{M} \sum_{n=1}^M \frac{\int_{t_n^s}^{t_n^e} q(t) dt}{\Delta t_n} \bigg|_{\text{wind},0}$$

where, suffix n is the index representing various overtopping cycles (there are M cycles considered in the simulation) with the duration Δt_n , i.e. $\Delta t_n = t_n^e - t_n^s$, where t_n^s and t_n^e are the start and end of the n^{th} cycle respectively in time. The purpose of this nondimensionalization is to understand how the inertia of the overtopping water with and without wind dominates over the underlying standing wave energy.

From Figure 7 we can clearly distinguish two regimes. Note that the Reynolds numbers $4.64\text{e}+06$, $3.1\text{e}+06$, $2.32\text{e}+06$ and $1.55\text{e}+06$ correspond to wind speeds 30, 20, 15 and 10 m/s, respectively. These values are chosen based on referral by Torbay council to available records of wind gusts during storm surge events at coastal areas like at Torbay, UK. It is seen in Figure 7 that in one of the regimes, the overtopping rate decreases with increasing wave steepness both in the absence of wind and when the wind speed is low. The reason of this behaviour is the standing wave instability discussed above. Recalling that while $H/d = 0.3$ and $ka = 0.3063$, we can refer to Figure 6 in order to see what happens when the impinging wave is unstable. The major portion of the water in the first triplet falls back to sea. We can also verify this strange reduction in overtopping rates with increasing steepness in Figure 7 by comparing them with prediction from the Bayonet GPE online tool (<https://www.overtopping.co.uk>) which provides probabilistic assessments of the rates based on a large database of field measurements. In another regime, when

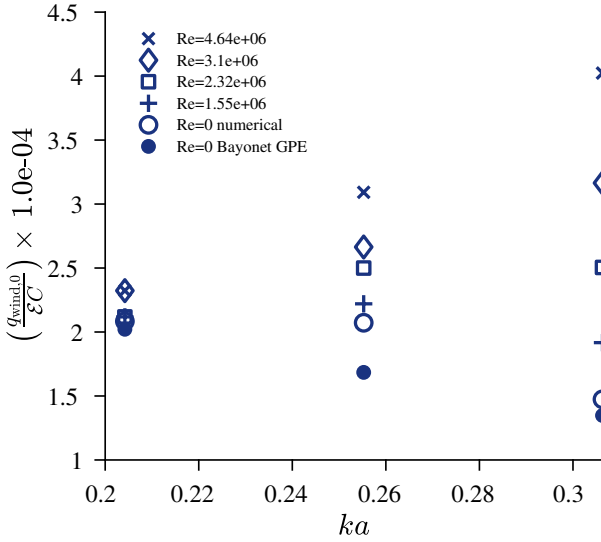


Figure 7. Variation of the overtopping volume flux with and without wind speeds over wave steepness.

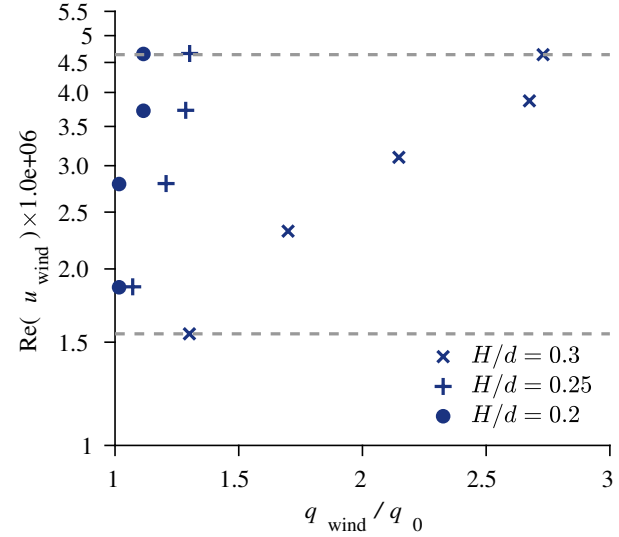


Figure 8. Amplification in overtopping rates with increase in wind speeds under different incident wave conditions, where the two horizontal lines refer to the two wind speeds considered in Figure 7.

wind speed is strong, the situation is exactly opposite, where the overtopping rate increases with increase in wave steepness. This is because the strong wind is able to significantly affect all the triplets uniformly and swept them away towards the onshore.

If we plot the amplification in the overtopping rates under different wind speeds in Figure 8, we can explain the amplifications using the above findings. Small wind speeds do not affect the overtopping at low wave steepness. Thus the amplification in overtopping rates is very close to unity at low H/d in Figure 8. However, with increase in wind speed, the amplification in overtopping rate takes place differently in different wave steepness. If the wave steepness is low, there is not much enhance in the amplification with increasing wind speed. However, at higher wave steepness, i.e. $H/d = 0.3$ in Figure 8, when the impinging wave is close to the instability, the first triplet which is otherwise remains unaffected in absence of or in low wind speed, now starts getting affected with increasing wind speed. As one can see, the overtopping rate amplification in the case of unstable standing wave regime ($H/d = 0.3$) may reach $q_{\text{wind}}/q_0 \approx 2.8$, much higher compared to stable standing wave regimes. If we refer to Figure 7, we can estimate the same value by taking ratio of the overtopping rate at $Re = 4.64 \times 10^6$ over the value at $Re = 0$ when $ka = 0.3063$.

4. Conclusions

The effect of wind speed on the wave overtopping at vertical coastal structures is studied in a wide range of regimes by varying the wave steepness. The air motion modelling the wind is introduced in the numerical model using the specifically designed pressure gradient correction term. Reflection of the incident wave from the coastal structure forms the standing wave in the near-shore region that may produce the water discharge to the coastal line. It is found that a small wind speed does not affect the discharge rate. If the standing wave is stable, the increase of the wind speed leads to the corresponding increase of the discharge rate, as one expects. Interestingly, at low to moderate wind speed the increase of the wave steepness shows the small reduction in the discharge rate that is not quite obvious.

The regime of wave reflection leading to loss of stability of the standing wave has previously been discovered by Longuet-Higgins and Drazen (2002) and confirmed in physical experiments. In the current research, this regime is identified in terms of wave steepness. Moreover, the form of impinging water jet at the vertical coastal structure is found to be closely related to the stability of the standing wave field. At the critical wave steepness, the overshooting jet conforms to a triplet where each third wave is the highest

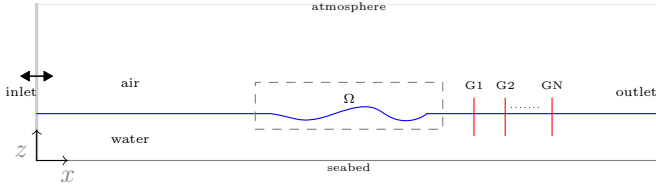


Figure 9. Schematic of the numerical water tank used for focused wave tests.

compared to the first one. Triggering standing wave instability results in significant change in the overtopping discharges over cycles and thus modifies the physical processes involved.

This quite fundamental finding needs further investigation to be adopted for practical use; for example, while studying the wave interaction with the vertical coastal defences during a full tidal cycle. In the presence of a strong wind (as usual in the case of a storm surge event) and if the impulse parameter \mathcal{I} becomes much smaller, the wave interaction with the defences in low tide may be as hazardous as in the high tide.

5. Acknowledgements

This project was funded and supported by the Natural Environment Research Council (NERC), UK under grant No. NE/R009155/1 and the Construction Industry Research and Information Association (CIRIA), UK, to whom we are very grateful. We are also grateful to partners K. Hu from Royal Haskoning DHV; M. Russell and S. Manson from Environment Agency; D. Stewart and M. Wood from Torbay Council and H. Winter and A. Joly from EDF Energy R & D UK Centre for providing several key input to the research.

A. Appendix: Validation of the numerical model: wind effects on focused wave

The schematic of NWT used for investigating the capability of the adopted model to simulate wind effects on focused wave is shown in Figure 9. A moving paddle at the inlet (by using the 'olaDyMFlow', [Higuera et al. \(2013\)](#)) is used to generate a very steep wave at a prescribed time and position (a focused wave) in the NWT. The origin of the coordinate system lies at the seabed and at the mean position (which is also the initial position) of the paddle. The motion of the paddle is governed by

$$(16) \quad S(t) = \sum_{n=1}^N \frac{a_n}{F_n} \cos(\omega_n t + \epsilon_n),$$

where F_n is the linear wave-to-paddle transfer function

$$(17) \quad F_n = \frac{2 [\cosh(2k_n d) - 1]}{\sinh(2k_n d) + 2k_n d}.$$

The wave number k_n and the frequency ω_n of n^{th} Fourier component are correlated through linear wave dispersion. We use $N = 32$ components with $\hat{\omega}_1 = 0.5$ and $\hat{\omega}_N = 1.4$. The phase of the n^{th} wave component is given by $\epsilon_n = k_n x_f - \omega_n t_f$, where $\hat{x}_f = 10$ and $\hat{t}_f = 31.32$ are the desired focusing points in space and time, respectively. The amplitude a_n of the individual components are set as A_t/N , and $\hat{A}_t = 0.256$. From the information on \hat{x}_f we can select the wind region Ω spreading over a few peak wave lengths, and the start and duration of the wind are set based on \hat{t}_f . The incoming wave is efficiently absorbed through the outlet. The wave field is tracked using the wave gauges G1, G2, etc. The time histories of wave elevation recorded at these gauges during the simulation are used to construct the amplification factor A defined as

$$(18) \quad A = \frac{H_{\max}}{H_0},$$

where $H_{\max} = \max(H_{\text{crest}}, H_{\text{trough}})$, and the two crest and trough are just one after the other. The average wave height H_0 is measured at the moving paddle in the time range $12 \leq \hat{t} \leq 37$.

The effect of the wind generated in the region Ω using the described above method is shown in Figure 10 for the wind speed 6 m/s (the velocity field is scaled almost by a factor 6 for better visualization). In this figure, red color corresponds to the water phase, $\alpha = 1$, while blue is the air phase, $\alpha = 0$. The wind flow separation from the free surface at the wave crest is seen, which is usual for the conditions considered in the simulation. This flow separation is typical for the case of well known wind sheltering and it is clear that the adopted model is successful to capture that effect. The comparison of the amplification factor as defined in equation (18) with experimental measurements of [Kharif et al. \(2008\)](#) is shown in Figure 11. For the range of the length along the NWT we consider, the calculation of A is found to be well predicted by our model while compared to the experimental measurement from [Kharif et al. \(2008\)](#). The average error is found to be around 8% and thus validates the pressure gradient correction method we use in our NWT to induce the wind motion in the region Ω . The amplification in this case is mostly due to the wind induced pressure distribution over the free surface and has already been well predicted by [Kharif](#)

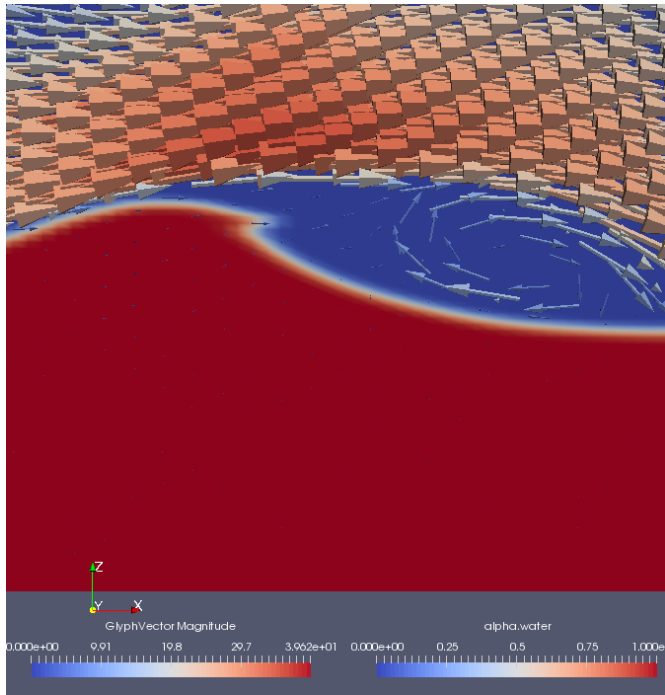


Figure 10. Wind flow generated in the region Ω .

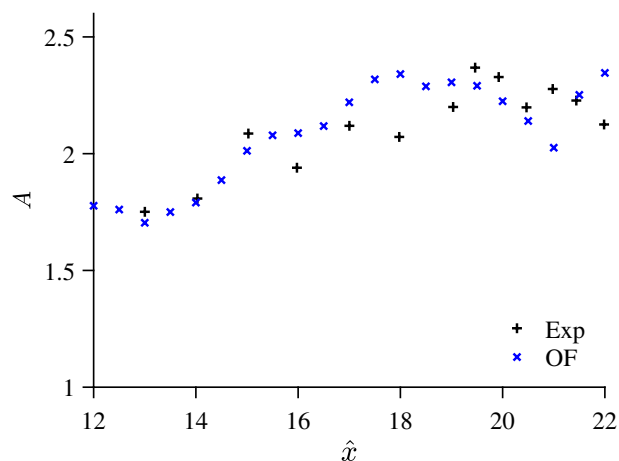


Figure 11. Comparison of amplification factor predicted by the numerical model OpenFOAM (OF) with the experimental measurements (Exp) by Kharif *et al.* (2008)

et al. (2008) using a potential flow model, where wind effects can be incorporated using a separate pressure term in the free surface boundary condition. The accuracy of this representation depends on type of interaction that takes place between air and water (e.g.

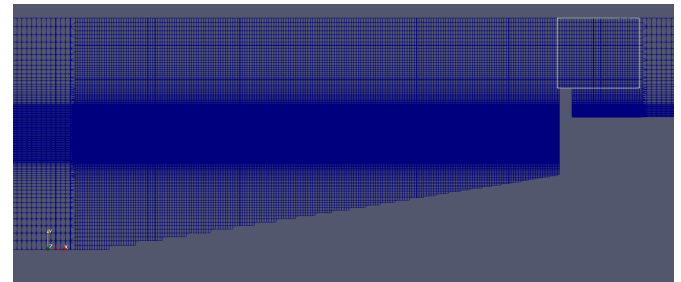


Figure 12. Mesh structure used near the sea defence and the free surface. The outline of the wind zone is shown above the defence.

whether there is a mixing or not) and local shape of the free surface profile.

It should be noted that the validation test adopted above is applicable at deep water where the breaking condition is emulated by focusing multiple wave lengths. The wind region covers the focus region. Whereas, in test cases described in the main part of this paper, the wind effects on overtopping are investigated in different depth conditions and using monochromatic waves. In both of these cases, the interaction is characterized by wind effects on large wave crests. Secondly, the resulting effect is desired within a small range from the place where most interactions take place. Thus, it is assumed that mechanism of wind effect is well represented in the overtopping cases as well.

B. Appendix: Convergence

The mesh structure is shown in Figure 12. The background mesh is quite coarse and we compress the mesh smoothly near the free surface based on the highest wave height we consider at the inlet in our simulations. The distribution of the cells along depth is as follows. Around 70% of the total number of cells used across depth is concentrated uniformly in the range covered by the wave crest to trough. Whereas, the remaining cells are distributed with an expansion ratio of 8 in the background, i.e. the cell height in coarse region (near the top and the sea bed) is eight times of that adjacent to the compressed region. Furthermore, the mesh near the sea defence and the sea bed slope is refined in order to better resolve the wave structure interaction during the overtopping. The time history of wave elevation measured at this defence under different mesh resolution used in the coarse background mesh in the horizontal direction is depicted in Figure 13 for a fixed aspect ratio

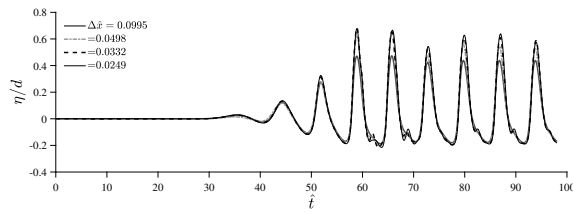


Figure 13. Time history of wave elevation measured at the sea defence at different mesh resolutions for incident wave condition $H/d = 0.25$ and $\hat{T} = 7$.

zone name	Ω_x/Δ_{jet}	elapsed CPU times (s)
wind zone 1	6.25	22487
wind zone 2	21.32	33213.6
wind zone 3	34.46	37498.3

Table 3. Execution times to simulate $70 \leq \hat{t} \leq 77$ for wind speed 30 m/s under three different wind zones. The length of the wind zone is represented by Ω_x .

$\Delta\hat{y}/\Delta\hat{x} = 0.2693$. The solution for the wave elevation is found to converge with the mesh resolution $\Delta\hat{x} = 0.0332$, and that is the mesh structure we use in the test cases discussed here.

The variation in the overtopping rates under three different lengths of the wind zone Ω is shown in Figure 14 for an overtopping cycle. The region referred as wind zone 1 is used in test cases here and it is found that further increase in the length of this region does not cause significant changes in the characteristics of the discharge. Execution time of these runs with different wind zones is summarized in Table 3. These tests are run in serial in a PC laptop (ASUS-Zephyrus-G502DU) with 24 GB RAM, 2.3 GHz AMD Ryzen processor. From Table 3, we can see that the simulation with the given wind speed is efficiently carried out using wind zone 1. Differences in run times under different lengths of the wind region are not that much significant in low wind speed compared to high wind speed.

REFERENCES

Bruce T, van der Meer J, Pullen T and Allsop W (2018) Wave overtopping at vertical and steep structures. In Y. C Kim (Ed.) *Handbook of Coastal and Ocean Engineering*, chapter 23, World Scientific : 633–661.

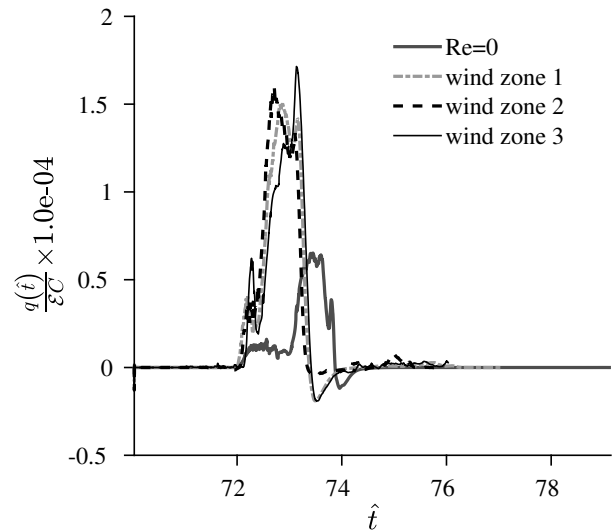


Figure 14. Time history of overtopping rates under different wind regions and no wind condition (i.e., Reynolds number $Re = 0$) for incident wave condition $H/d = 0.3$ and $\hat{T} = 7$ and wind speed 30 m/s ($Re = 4.64e + 06$).

Chalikov D (1978) The numerical simulation of wind-wave interaction. *J Fluid Mech* **87**: 561–582.

Chen XY, Tsai CP and Hwung HH (1988) The Theoretical Studies on Nonlinear Standing Waves. In K. Horikawa, H. Maruo (Eds) *Nonlinear Water Waves, IUTAM Symposium* : 135–142.

De Chowdhury S, Causon D, Qian L, Mingham C, Chen H, Lin Z, Zhou JG, Pullen T, Silva E, Hu K, Russel M, Manson S, Winter H, Joly A, Stewart D and Wood M (2019) Investigation of wind effects on wave overtopping at sea defences. In N. Goseberg, T. Schlurmann (Eds) *Proc: Coastal Structures* : 841–850.

De Rouck J, Geeraerts J, Troch P, Kortenhaus A, Pullen T and Frnaco L (2005) New results on scale effects for wave overtopping at coastal structures. In N. W. H. Allsop (Ed) *Proc: Int Conf on Coastlines, Structures and Breakwaters* (2005) .

De Waal JP, Tönjes P and van deer Meer. J (1996) Wave overtopping of vertical structures including wind effect. In B. L. Edge (Ed) *Proc: 25th Coastal Engineering Conference* : 2216–2229.

González-Escrivá JA, Garrido JM, Medina JR and Geeraerts J (2004) Laboratory real storm reproduction using wind. In J. M. Smith (Ed) *Proc: 29th Intl. Conf Coast Eng* **1**: 677–689.

-
- Hasan SA, Sriram V and Paneer Selvam R (2018) Numerical modelling of wind-modified focused waves in a numerical wave tank. *Ocean Eng* **160**: 276–300.
- Hieu PD, Vinh PN, Toan DV and Son NT (2014) Study of wave-wind interaction at seawall using a numerical wave channel. *Appl Math Model* **38**: 5149–5159.
- Higuera P, Lara J and Losada IJ (2013) Realistic wave generation and active wave absorption for Navier-Stokes models: Application to OpenFOAM[®]. *Coast Eng* **71**: 102–118.
- Issa R (1985) Solution of the implicitly discretized fluid flow equations by operator-splitting. *J Comput Phys* **62**: 40–65.
- Jacobsen NG, Fuhrman D and Fredsoe J (2012) A wave generation toolbox for the open-source CFD library OpenFoam[®]. *Int J Numer Meth Fl* **70(9)**: 1073–1088.
- Kharif C, Giovanangeli JP, Touboul J, Grare L and Pelinovsky E (2008) Influence of wind on extreme wave events. *J Fluid Mech* **594**: 209–247.
- Li T and He W (2011) Numerical simulation of wind effects on wave overtopping by a two-phase solver. In *Proc: Twenty-first International Offshore and Polar Engineering Conference* : 903–909.
- Longuet-Higgins MS and Drazen A (2002) On steep gravity wave meeting a vertical wall: a triple instability. *J Fluid Mech* **466**: 305–318.
- Miles J (1957) On the generation of surface waves by shear flows. *J Fluid Mech* **3**: 185–204.
- Oliveira P and Issa R (2001) An improved piso algorithm for the computation of buoyancy-driven flows. *Num Heat Transf B* **40**: 473–493.
- Van der Meer J, Allsop NWH, Bruce T, De Rouck J, Kortenhaus A, Pullen T, Schüttrumpf H, Troch P and Zanuttigh B (2018) EurOtop. manual on wave overtopping of sea defences and related structures. an overtopping manual largely based on european research, but for worldwide application. www.overtopping-manual.com.
- van Gent MRA, Van den Boogaard H, Pozueta B and Medina JR (2007) Neural network modelling of wave overtopping at coastal structures. *Coast Eng* **54**: 583–593.
- Ward D, Wibner CG and Zhang J (1998) Runup on coastal revetments under the influence of onshore wind. *J Coastal Res* **14(4)**: 1325–1333.
- Ward D, Zhang J, Wibner CG and Cinotto CM (1996) Wind effects on runup and overtopping of coastal structures. In *B. L. Edge (Ed) Proc: 25th Coastal Engineering Conference* : 2206–2215.
- Wolters G and van Gent MRA (2007) Maximum wind effect on wave overtopping of sloped coastal structures with crest elements. In *L. Franco, G. R. Tomasicchio and A. Lamberti (Eds.) Proc: 5th Coastal Structures* : 1263–1274.
- Xie Z (2014) Numerical modelling of wind effects on breaking solitary waves. *Eur J Mech B- Fluid* **43**: 135–147.
- Yan S and Ma Q (2010) Numerical simulation of interaction between wind and 2D freak waves. *Eur J Mech B- Fluid* **29**: 18–31.